THE JOURNAL OF PHYSICAL CHEMISTRY C
A JOURNAL OF THE AMERICAN CHEMICAL SOCIETY

pubs.acs.org/JPCC

Article

Thermal Conductance between <6 nm Single-Walled Carbon Nanotube Bundle and Si Substrate

Ibrahim Al Keyyam, Mahya Rahbar, Enzheng Shi, Baini Li,* Tianyu Wang,* and Xinwei Wang*

Cite This: *J. Phys. Chem. C* 2024, 128, 1505−1517

Read Online

ACCESS | Metrics & More | Article Recommendations

ABSTRACT: Interfacial thermal conductance between a single-walled carbon nanotube (SWCNT) and substrate is rarely characterized and understood due to substantial challenges in probing the energy transport across such nm-wide contact. Here, we report the interfacial thermal conductance between a <6 nm thick SWCNT bundle and Si substrate. The energy transport state-resolved Raman is employed for the measurement, where the Raman spectrum change under continuous wave (CW) and 20 ns pulsed laser heating is measured for the thermal response of the SWCNT under steady and transient heat conduction sustained by the interfacial thermal conductance. Since no knowledge is needed for laser absorption and temperature rise of the sample, the measurement achieves extreme capability and confidence. For three locations of the SWCNT bundle, the interfacial thermal resistance is measured to be $(2.98 \pm 0.22) \times 10^3$, $(3.01 \pm 0.23) \times 10^3$, and $(1.67 \pm 0.27) \times 10^3$ K m W^{-1}, corresponding to thermal conductance in a range $(3.3-6.0) \times 10^{-4}$ W m^{-1} K^{-1}. Our analysis suggests a loose contact between the SWCNT bundle and the Si substrate, mainly attributed to the obvious nonuniformity of the sample, which was resolved by atomic force microscopy and Raman spectroscopy. For an assumed contact width of ∼1 nm, the interfacial thermal resistance would be of the order of 10^{-6} W m^{-2} K^{-1}, in line with those reported for mechanically exfoliated graphene and two-dimensional (2D) materials.

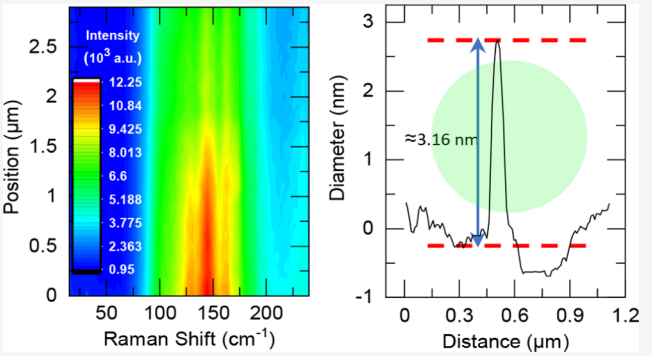

1. INTRODUCTION

Significant efficiency advancements have been made in nanoscale devices over the last 30 years. Take transistors, for example; despite this progress, the room for improvement is about 3 orders of magnitude of their current efficiency, up to the so-called fundamental physical limit, which is estimated to be around $3k_BT \simeq 10^{-20}$ J at room temperature.[1] As miniaturization advances, energy dissipation in nanoelectronics becomes a limiting factor that affects storage density and computational efficiency.[2] Consequently, the study of thermal transport phenomena at the nanoscale has attracted the attention of numerous researchers.[3] The extraordinary thermal properties of low-dimensional materials[4−6] present a promising avenue for potential solutions,[7] and the last two decades have seen tremendous progress in material science, leading to a deeper understanding of low-dimensional materials like carbon nanotubes (CNTs) and graphene.[8] These materials have demonstrated exceptional properties through experimental and theoretical evidence, positioning them as the future of several industries, including semiconductors.[9,10] CNTs have been the subject of much interest since their discovery in 1991[11] due to their unique properties. Their extraordinary structural properties are explained by strong carbon−carbon covalent bonding. Their electronic structure is similar to graphene, with the sp^2 hybridization, yet due to the periodic boundary condition along the circumference, a band gap could be achieved, making them either semiconducting or metallic. CNTs are also highly valued for their exceptional thermal conductivity, which has been confirmed experimentally for multiwalled carbon nanotubes (MWCNT) and individual single-walled carbon nanotubes (SWCNT).[12]

A variety of techniques have been used to characterize the interfacial thermal resistance (ITR), from computational methods[13−17] to experimental techniques like the microbridge method,[18] contact transient electrothermal (CTET),[19] time-domain thermal reflectance (TDTR),[20] and so on. However, reported values often show discrepancies and lack consistency due to the difficulty of measuring interfacial thermal conductance at contact lengths of a few nanometers or even less and the different uncertainty levels introduced by each

Received: November 16, 2023
Revised: December 27, 2023
Accepted: December 30, 2023
Published: January 11, 2024

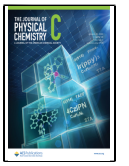

technique. Pop et al. investigated the electrical and thermal properties of metallic single-wall carbon nanotubes (SWCNTs) on insulating substrates. They deduced a thermal conductance between SWCNT and the substrate as 0.17 ± 0.03 W m^{-1} K^{-1}. They also revealed that electrons contribute less than 15% of the total thermal conductivity of metallic nanotubes at room temperature.[21]

Maune et al.[22] reported the ITR between SWCNT and sapphire substrate of around 3 K m W^{-1}, dominated by interfacial resistance. Their results suggest that a relatively short contact length of around 10−30 nm is sufficient to transfer heat efficiently into nanotubes. Yang et al.[23] measured the contact thermal resistance between multiwalled carbon nanotubes (MWCNT). They found that the contact thermal conductance can increase by nearly 2 orders of magnitude as the contact area increases from a cross-contact to an aligned contact. Their results yielded a thermal contact resistance in the order of 10^{-9} K m^2 W^{-1} at room temperature, 1 order of magnitude lower than that from a molecular dynamics simulation in the literature. In a more recent study, the thermal resistance through cross-contacts between individual MWCNT was investigated by Yang et al., and it was found that the normalized contact thermal conductance per unit area depends linearly on the tube diameter, contrary to common expectations. They reported a cross-contact interfacial thermal conductance that ranges from 3×10^8 to 1.3×10^9 W m^{-2} K^{-1}. These results were supported and extended through molecular dynamics simulations with multilayer graphene nanoribbons. The findings suggest an unexpectedly long phonon mean free path in the *c*-axis direction of graphite. Phonon reflection at free surfaces could explain the observed behavior.[23] One possible source for the variation in the reported values is the different contact areas estimated by researchers. Thus, a thermal contact resistance per unit length is more favorable.[24]

For characterizing materials at the nanoscale, the Raman-based techniques offer the advantage of minimal sample preparation and small spatial resolution with comparable uncertainties as in other methods.[25] Despite these advantages, Raman-based measurements can still have several sources of errors, yet they can be minimized. As comprehensively discussed in their review, Xu et al.[26] revealed that the stress induced by thermal expansion mismatch during calibration could cause errors when using Raman spectroscopy to measure the temperature change across the interface. Therefore, the temperature coefficients of the Raman properties determined during calibration may introduce unknown errors. Moreover, the measurement of laser absorption can be affected by the spacing between the sample and the substrate, which can vary depending on the thickness of the sample and the preparation method, leading to sample-specific absorption coefficients. To address those uncertainties, the energy transport state-resolved Raman (ET-Raman) technique was first introduced by Wang's group[27] and is used in this work. This technique involves creating two energy transport states, a steady state achieved by using a continuous wave (CW) laser and a transient state by using a pulsed laser. The ITR can be determined by comparing the Raman shift variations measured in time and space domains from different energy transport states. Therefore, this method can potentially eliminate errors arising from the Raman property temperature coefficient calibration.[28] The technique has been further extended by Zobeiri et al.,[29] who proposed using two energy transport states: a CW laser for steady-state energy transport and an amplitude-modulated laser at frequency (f) for transient energy transport state. An essential advantage of this method (termed the frequency domain ET-Raman, or FET-Raman) is the ease of obtaining a good signal. However, the ET-Raman provides more sensitive probing measurement since the laser pulses almost have no interference with each other.

We note here that ET-Raman has some limitations and cannot be used to characterize all types of materials (i.e., metallic, semiconducting, and dielectric). For a sound Raman spectrum, light should be absorbed, either by some electronic transition as in semiconductors with bandgaps below the photon energy or by photon-phonon interactions, which are more complicated due to spin conservation. For metallic samples, the valence electrons respond to photons and move freely within the valence band. This puts a limit on the phonon activity induced by the laser absorption. Hence, metallic samples cannot be characterized using ET-Raman or any other conventional Raman-based techniques. In summary, if a material has a sound Raman spectrum and laser absorptivity to induce heating, then ET-Raman can be implemented for thermal characterization.

Here, we report the ITR per unit length for single-walled carbon nanotubes (SWCNT) on a silicon (Si) substrate. To the best of our knowledge, this is the first study to attempt this method for these materials. We believe that this would eliminate the possible errors arising from estimating the interface's contact area and therefore provide intrinsic insights about the interface between CNTs and Si substrate. Our novel approach, the ET-Raman technique has been described in detail and aims to minimize the uncertainties associated with laser absorption measurements and Raman temperature calibration. In this work, we differentiate the thermal energy transport mechanism for our sample under laser heating by switching between a continuous wave laser beam (CW) and an amplitude-modulated nanosecond pulsed beam, thereby enabling a unique temperature rise to be induced in the SWCNT. The resulting Raman signals are then analyzed with laser powers adjusted to generate experimentally measurable Raman signal red shifts. The ET-Raman approach requires only relative Raman signal red shift information, thereby eliminating the need for a sample-dependent Raman temperature coefficient and light interference effects at the interfacial gap. A physical model is developed to extract the ITR. More details will be provided in upcoming sections.

2. MATERIALS AND METHODS

2.1. Material Synthesis. The CNTs are synthesized using atmospheric pressure chemical vapor deposition (APCVD) with sulfur, ferrocene, and xylene as initiator materials. To compile the CNT films, a nickel foil is placed downstream of a quartz tube. The CVD furnace is first heated to 1160 °C under a stream of 20 sccm of 99.999% pure Ar gas. A solution of sulfur (0.001 g mL^{-1}) and ferrocene (0.045 g mL^{-1}) dissolved in xylene is then injected into the upstream side of the quartz tube at a flow rate of 5 mL min^{-1} at 1160 °C furnace temperature. At the same time, the carrier gas is changed to a mixture of Ar and H_2 (V_{Ar}/V_{H_2} = 0.85:0.15) and the flow rate is increased to 1500 sccm. In order to control the thickness of the CNT films, the reaction time is changed from 5 to 60 min. The grown CNT films float downstream and are collected on nickel foil. The CNT film could be easily removed from the nickel foil and placed on a silicon (Si) substrate.

https://doi.org/10.1021/acs.jpcc.3c07572
J. Phys. Chem. C 2024, 128, 1505−1517

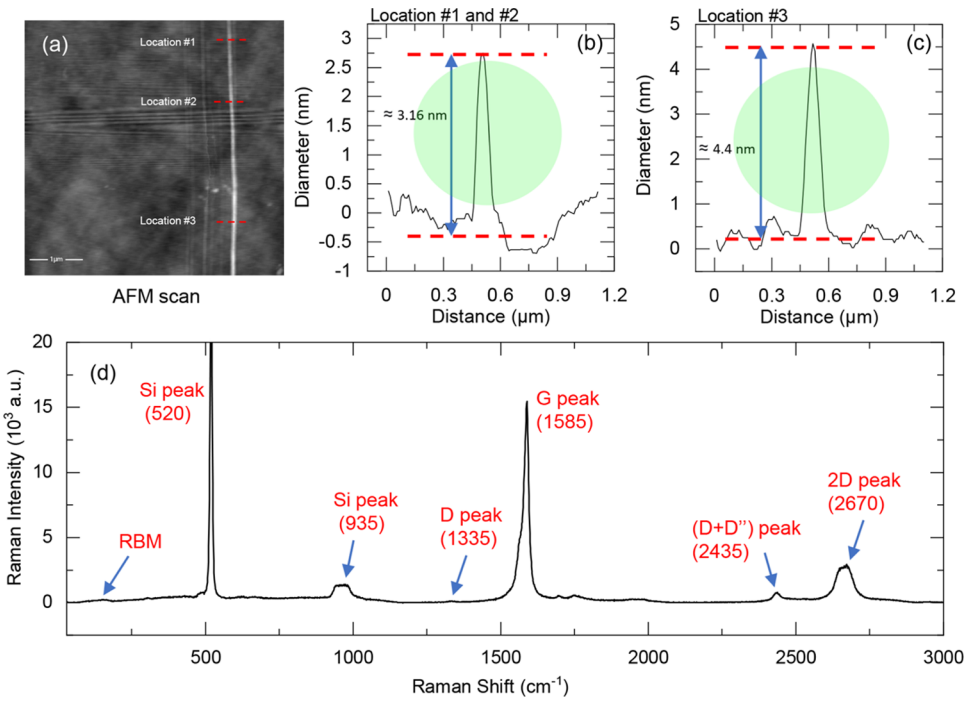

Figure 1. (a) AFM scan image. (b, c) Height of the sample corresponding to the red dashed lines in the AFM scan image, with the green shaded area representing the laser spot in ITR measurement. (d) Full Raman spectrum of the sample.

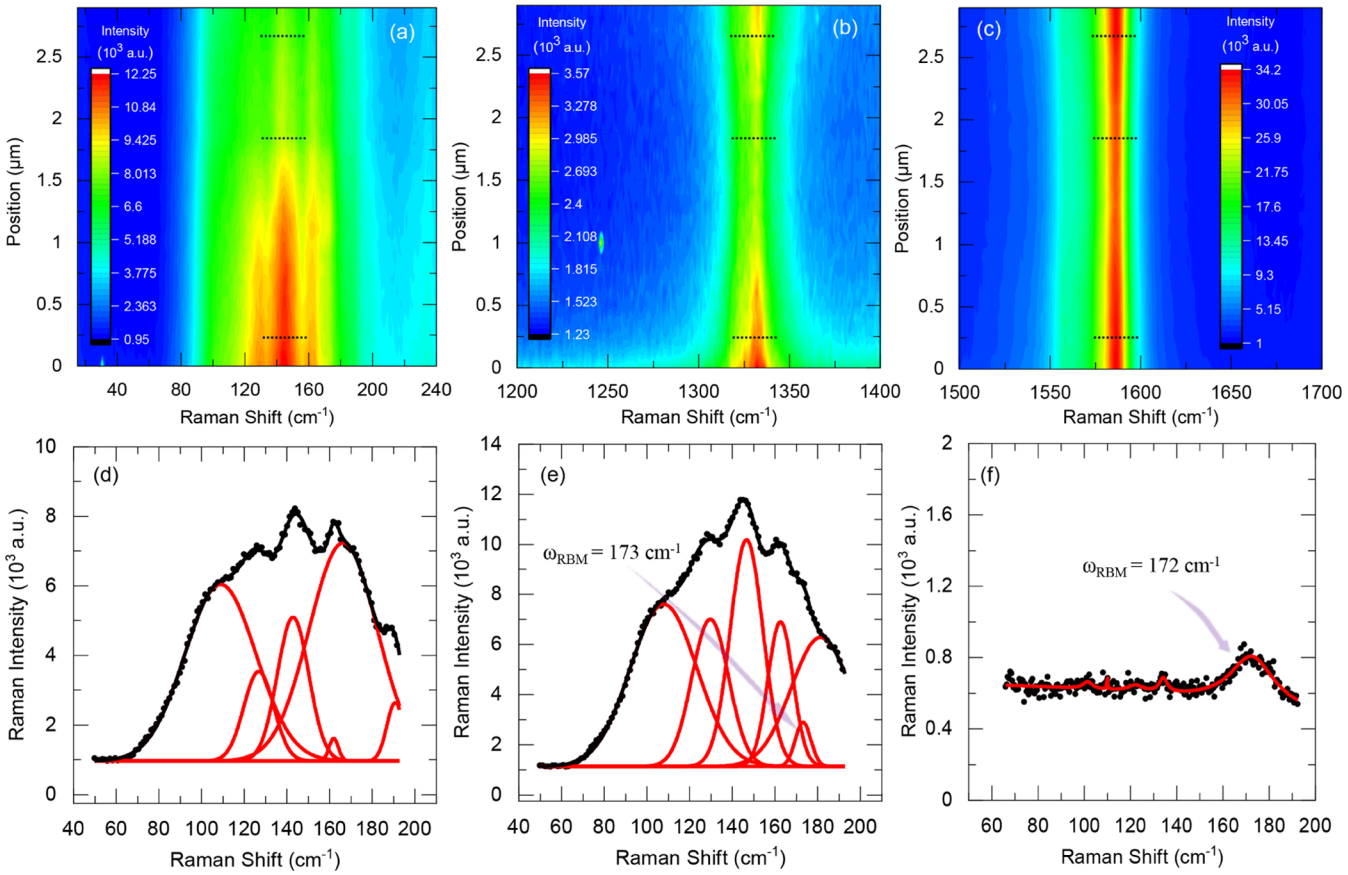

Figure 2. (a) RBM scan, (b) D band scan, and (c) G band scan. The black dashed lines correspond to the locations shown in Figure 1a. The multiple peak fitting using Gaussian function for the RBM spectrum of the first location using 532 nm laser for (d) locations #1 and #2, (e) location #3, and (f) the RBM excitations of the third location using 785 nm laser.

https://doi.org/10.1021/acs.jpcc.3c07572
J. Phys. Chem. C 2024, 128, 1505−1517

2.2. Experimental Setup. HORIBA Scientific's confocal Raman microscope is coupled to the spectrometer iHR 550 and to the laser source Excelsior 532 nm CW laser, which is used to achieve steady-state heating. The transient state, however, is achieved by using a Tetronix AGF31000 function generator to modulate the signal. The focused laser spot size is measured by the knife-edge method, which yielded a radius of 0.38 μm. The sample is mounted on a 3-axis NanoMax 300 motorized nano stage under the 100× objective lens. To control the irradiated laser power on the sample, a motorized neutral density (ND) filter is implemented. For a more precise and faster experiment, all of the components are controlled through a LabVIEW program.

2.3. Material Characterization. The profile of the studied area of the sample is characterized using atomic force microscopy (AFM). The AFM scan image of the SWCNT sample in Figure 1a, obtained using the contact mode, provides essential insights into the sample's characteristics. Three different locations are studied, as marked in Figure 1a. First, it confirms the presence of only one SWCNT bundle within the laser spot domain, as it is confirmed by Figure 1b,c. This ensures that the Raman spectrum obtained during the experiment belongs to one sample, eliminating uncertainties that could arise from multiple samples being subjected to different effective laser intensities due to the Gaussian shape of the laser spot. Second, the scan reveals that the diameter of the bundle is not constant, with AFM measurements indicating a reduction in the height from 4.4 to 3.16 nm. The Raman scanning for the radial breathing mode (RBM), D, and G peaks confirms this nonuniformity and will be discussed in further detail.

The radial breathing mode (RBM) peaks provide valuable information on the diameter(s) of the SWCNTs within the bundle.[30,31] It is a vibrational mode that is symmetric in nature and arises from the oscillations of carbon atoms in the radial direction perpendicular to the tube axis. It has been established in previous research that the frequency of RBM is inversely proportional to the diameter of the tube, as given by the relation $\omega_{RBM} = (A/d) + B$, where A and B are constants that have been determined experimentally for different configurations. For instance, freestanding CNTs were found to have constants of $A = 204$ cm^{-1} nm and $B = 27$ cm^{-1}[32] while bundled nanotubes have constants of $A = 239$ cm^{-1} nm and $B = 0$ cm^{-1}.[33] Various other configurations have also been reported in the literature.[34,35] In addition to the sensitivity of the RBM frequency to the diameter and chirality of SWCNTs, the line width of the RBM offers valuable insights. The RBM broadening along the tube axis is closely linked to the diameter distribution and chirality of SWCNTs within the sample.[36] However, this phenomenon is only true when the laser energy is fixed,[37] which is the case in our scanning process. To sum it up, when the laser energy is fixed, a wider RBM peak denotes a broader range of CNT diameters in the sample. The RBM scan in Figure 2a confirms the diameter variation observed in the AFM measurements, showing a noticeable variation in the line width. As discussed and illustrated in Figure 1b,c, the AFM measurements revealed a height of 3.16 nm at locations #1 and #2 and 4.4 nm at location #3. By utilizing the AFM measurements and the frequency-diameter relationship above, we can determine the diameters of individual SWCNTs within each bundle, enabling the evaluation of the number of carbon nanotubes within the bundle. A comprehensive analysis is provided in Section 3.

More information can be extracted from the Raman spectrum. The D peak shows a highly dispersive feature, meaning its frequency is sensitive to laser energy. Although the scan in Figure 2b is conducted at a fixed laser energy, the D peak shows a slight frequency shift along the tube axis. This behavior is consistent with previous reports by Pimenta et al.,[38] who showed that the frequency of the D peak is related to the tube diameter: smaller diameter tubes exhibit lower frequencies. Moreover, they indicated that the intensity variation of the D peak could result from multiple factors such as lattice defects, finite tube size, and varying resonance conditions among tubes. As a result, no definitive conclusion can be drawn. Nonetheless, the nonuniformity of the scanned sample is evident and aligns with previous observations. The full-width at half-maximum (fwhm) of the D peak is indicative of the defect distribution within the sample,[39] although it is insufficient to identify the specific defect type. Therefore, further investigation is necessary. Overall, the scan confirms the nonuniformity of our sample.

The quality of the sample under investigation is a critical factor in the interpretation of the Raman spectra. As depicted in Figure 1d, the D peak intensity is notably low, which has been widely documented as an indicator of high sample quality.[40] Further evidence supporting this claim is observed in the Raman band (D + D″) situated around 2435 cm^{-1}, which is identified as another double-resonance process akin to the 2D band at 2670 cm^{-1} and was first analyzed by the Dresselhaus group.[41] A thorough review by Dresselhaus et al.[42] emphasized that this peak is exclusively present in high-quality samples and proper experimental setups. Our findings confirm this assertion where the peak intensity remains unaltered under varying laser power conditions, consistent with results previously reported by Shimada et al.[41] Unlike the D band, the G band is insensitive to the change in the tube diameter or chirality.[42] This is confirmed in Figure 2c, which shows a constant wavenumber along the tube. The line width, on the other hand, carries information on the electronic structure of the SWCNTs. The Lorentzian shape for the G band, as observed in the Raman spectrum, indicates semiconducting individual SWCNTs. This observation is in immense agreement with the tight binding calculations for the energy gaps of semiconducting SWCNTs. A more in-depth discussion will be presented in Section 3. As mentioned before, the G peak exhibited the largest signal-to-noise ratio and was used to deduce the Raman shift power coefficient.

The phenomenon of size shrinking in carbon nanotubes is multifaceted and can be attributed to various factors. One possible explanation is that the overall bundle size has decreased due to alterations in the intertube interactions caused by van der Waals forces. The mechanism behind this is the following: as the intertube distance decreases, the van der Waals forces between different tubes increase as it is proportional to $\sim r^{-7}$.[43] This increase leads to stronger attraction between the tubes, resulting in further contraction of the bundle diameter. As shown in previous studies, the van der Waals interactions are also known to play a significant role in the self-assembly of SWCNT bundles.[44] Another proposition is that the individual SWCNTs have undergone a reduction in diameter due to the change in the distribution of defects, including differences in chirality, defects, or impurities within the nanotube during the growth phase. The concentration of defects has been extensively studied by Yuzvinsky et al.,[45] who have demonstrated that precise control

https://doi.org/10.1021/acs.jpcc.3c07572
J. Phys. Chem. C 2024, 128, 1505−1517

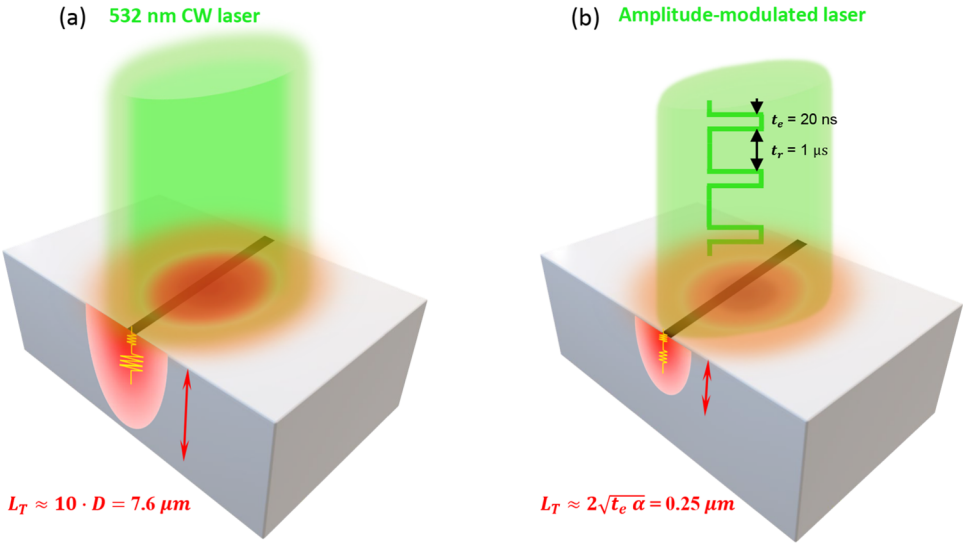

Figure 3. (a) Steady-state energy transport schematic using a CW laser with a 532 nm wavelength. The diffusion length extends throughout the substrate. (b) Schematic of the transient energy transport state using an amplitude-modulated CW laser with 532 nm wavelength. The heating time (t_e) is set to 20 ns, whereas the cooling time (t_r) is set to 1 μs. The thermal diffusion length is finite and much shorter than the steady-state scenario. By comparing the steady-state energy transport response to the transient one, the ITR can be effectively measured.

over SWCNT diameter could be achieved by regulating defects. It is, however, essential to note that these two scenarios are not mutually exclusive, meaning that the observed situation may be a superposition of both effects. Such variations in diameter can significantly affect the electronic and mechanical properties of nanotubes.

2.4. Theoretical Development of ET-Raman Technique and the Heat Conduction Model. The ET-Raman technique in this research involves using a CW laser and a nanosecond pulsed laser (obtained by amplitude modulating the CW laser) to expose the sample and analyze its thermal response. By acquiring the excited Raman signals during laser heating, we can obtain the temperature profile of the material, which needs not be its actual temperature rise. In this work, we establish two distinct energy transport states to investigate the interfacial energy transport between the SWCNT and the Si substrate. The ET-Raman process involves using a CW laser with a wavelength of 532 nm (corresponding to photon energy E = 2.33 eV) as a heat source for the SWCNT to probe it. A 100× objective lens is employed to focus the laser beam onto the sample. The laser spot size ($r_o \sim 0.38\ \mu$m), as shown in Figure 1b,c, is much larger than the SWCNT bundle diameter. The in-plane thermal diffusion along the SWCNT outside the laser heating area is still taken into consideration in our theoretical model to achieve high precision. More details are in Section 3.

During CW irradiation, the sample is heated to a steady-state rate. Here we increase the laser power (P) while recording the Raman signal to examine the temperature profile under different heating states. The Raman shift (ω) is red-shifted as we increase the laser power. Hence, the Raman shift power coefficient (RSC) is then obtained by taking the change in ω with respect to the laser power P ($\psi_{CW} = \partial\omega/\partial P$). The RSC is applied to the first-order G peak Raman active modes of the SWCNT, which appear as a single prominent peak at around 1582 cm^{-1} in the Raman spectrum. The G peak is chosen due to its highest signal-to-noise ratio among the entire spectrum. The laser power range is kept relatively low, while a linear relation is achieved between ω and P. It is worth noting that the RSC for a single energy state (i.e., the steady state or the transient state) is still a function of the laser absorption coefficient (α_L), Raman temperature coefficient ($\partial\omega/\partial T$), and interfacial thermal resistance (R'). In ET-Raman, the ratio of ψ is used as $\Theta = \psi_{tr}/\psi_{CW}$ for determining the ITR. Here, ψ_{tr} is for the transient state under pulsed laser heating and Raman scattering. As a result, the ET-Raman technique eliminates the effects of laser absorption and the Raman temperature coefficient, as explained in the following section. Therefore, the ITR is the only remaining unknown variable of interest.

In order to conduct a practical ET-Raman experiment using a pulsed laser, it is vital to consider the repetition rate or the time interval between pulses. If the goal is to observe transient states of heat conduction, ensuring the material has enough time to cool to ambient temperature between consecutive pulses is crucial. This is necessary to distinguish the CW steady-state heating from the transient heating caused by nanosecond pulsed lasers. Accurate measurement of the ITR becomes much more sensitive with this differentiation of thermal transport. If the repetition rate is too fast and the interval between pulses is too short, pulsed laser heating becomes more like CW laser heating. This is because the accumulated temperature increase throughout multiple pulses will have a more significant impact on the overall thermal transport of the system, which can mask the presence of ITR. Therefore, in order to effectively study transient states of heat conduction, it is essential to carefully design the experiment with an appropriate repetition rate that allows for sufficient time for the material to cool down between pulses.

In this work, 20 ns of heating time is chosen to achieve transient heating. To ensure the material returns to its initial temperature, a 1 μs off time is selected. It is important to note that the exact values may require adjustment based on specific experimental conditions and SWCNT properties. Given this relatively high repetition rate (~980 kHz), we employ a photodiode to discern variations in the intensity of the received signal, which may arise from distortion or other types of interference encountered during signal transmission. The results confirm a consistent and uniform pattern of intensity

https://doi.org/10.1021/acs.jpcc.3c07572
J. Phys. Chem. C 2024, 128, 1505−1517

that maintained a square shape, signifying faultless transmission of the laser beam.

Here, we note that our theoretical model based on the finite-volume method accounts for the number of heating cycles and the laser off time. By fixing the laser off time at a given value, we compare the temperature increase of multiple heating pulses to a single heating pulse. If the temperature rise is different (i.e., the temperature rise is higher for multiple heating cycles), then the heat is effectively accumulating and the relaxation time is not sufficient to cool the sample down to its initial temperature (i.e., room temperature). By iterating this, the laser off time can be optimized before running the experiment. We note that even if the material did not restore its initial temperature completely during the experiment (i.e., we underestimated the necessary thermal relaxation time), our theoretical model takes that into consideration, as pointed out above through multiple heating cycles. Nevertheless, we make sure to have sufficient relaxation time to obtain more distinct energy transport states and, hence, more sensitive probing.

The schematic diagram in Figure 3 shows a comparison between the steady-state response and the transient one. The thermal diffusion length (L_T) describes the distance over which heat diffuses through a material within a specific time interval. For steady-state heating with a CW laser, the thermal diffusion length is practically infinite, whereas, for the transient state, it can be evaluated using the formula $L_T = 2\sqrt{\alpha t_e}$, where α is the thermal diffusivity of the substrate and t_e is the laser pulse width. The value is estimated to be 0.25 μm by using this formula for the Si substrate. It is notable that the contribution of substrate thermal resistance to the overall thermal resistance is expected to be more significant in the steady-state case than in the transient one. This can be explained by the steady temperature distribution, where heat can diffuse throughout the material over a longer distance. Conversely, the contribution of the ITR to the overall thermal resistance is expected to be greater in the transient state than in the steady state. This is confirmed by calculating the thermal resistance in the substrate using $L_T/(\kappa_s a)$, where a is the contact width taken to be 1 nm and κ_s is the substrate thermal conductivity which is taken to be 148 W m^{-1} K^{-1}. Using the previous equation, the substrate thermal resistance in the transient state yields a value per unit length of around 1.7 K m W^{-1}. On the other hand, in steady-state heating, the substrate thermal resistance can be evaluated using the appropriate shape factor. To estimate the thermal conduction resistance and compare it to the ITR, we approximate the CNT as an infinitely thin rectangle of width a and length L on a semi-infinite medium. The unit length (L = 1 m) resistance can be calculated as $L_c/(0.932{\cdot}\kappa_s{\cdot}A_s)$,[46] where A_s is the active area and defined as $A_s = 2aL$ and L_c is the characteristic length defined as $L_c = (A_s/4\pi)^{1/2}$. By substituting the values, we calculated the substrate thermal resistance in the steady state to be 45.73 K m W^{-1}. It is evident that in both scenarios, the substrate thermal resistance is orders of magnitude less than the ITR determined experimentally in this work, which is found to be on the order of 10^3 K m W^{-1}. We note that this approximation has been made only to estimate the thermal conduction resistance and has not been implemented in our theoretical model as will be discussed shortly. To sum it up, the resistance at the interface is what governs the heat conduction at the nanoscale and is more prominent in the transient state. Hence, the temperature rise in the substrate is nearly negligible which validates our assumption in the theoretical model. More details will be provided in Section 3. It is, however, important to point out that the two energy transport states (i.e., the steady state and the transient state) are still both crucial to eliminate the dependence on the optical and thermal properties of the sample such as the laser absorption coefficient and the Raman temperature coefficient.

In the present study, to achieve precise determination of the ITR, our theoretical model takes into consideration the heat transfer along the tube direction, reducing the errors that would arise from assuming a one-dimensional (1D) heat conduction model in the thickness direction. The governing equation for the steady state and the transient state heat transfer are given as in eqs 1 and 2, respectively

$$\kappa\frac{\partial^2 T}{\partial x^2} - \frac{T - T_s}{R'{\cdot}A_c} + \dot{q} = 0 \tag{1}$$

$$\kappa\frac{\partial^2 T}{\partial x^2} - \frac{T - T_s}{R'{\cdot}A_c} + \dot{q} = \rho c\frac{\partial T}{\partial t} \tag{2}$$

Here, κ denotes the thermal conductivity of the sample, which is taken to be 50 W m^{-1} K^{-1} at room temperature as measured by our recently published work[47] for a suspended CNT of the same branch, ρ is the density, c is the specific heat, T_s is the substrate temperature, and A_c is the solid cross-sectional area of the CNT. The right-hand side of eq 2 represents the transient response. The first term on the left-hand side represents the heat conduction along the tube in the x-direction (axial direction), while the second term represents the heat transfer in the thickness direction (termed "z-direction" hereafter) from SWCNT to the Si substrate. We note that ballistic heat conduction in the axial direction, if it exists, will need a different treatment as the constructed physical model does not capture it. However, the thermal conductivity as measured reveals a phonon mean free path much smaller than the laser spot size. Ballistic conduction reported in the literature was associated with thermal conductivity in the range 2000−3000 W m^{-1} K^{-1} for CNT, which could yield a phonon mean free path long enough to be comparable to the laser heating area. Hence, no ballistic heat conduction in the axial direction is expected in our measurement. As shown in the equation, the heat transfer in the z-direction is a function of the ITR only, which is confirmed by our calculations in the previous section. To explain the underlying physics behind our assumption, the high thermal conductivity of carbon nanotubes, coupled with their very small thickness, leads to a very low Biot number (Bi) defined as $Bi \sim 1/(R'{\cdot}\kappa_r)$, where κ_r is the effective thermal conductivity of the CNT along the circumferential direction. As detailed later, R' is in the order of 10^3 K m W^{-1} and κ_r would be in the order of 1 W m^{-1} K^{-1}. Therefore, we have $Bi \ll 1$, indicating the validity of neglecting the spatial variation of temperature in the cross section of the SWCNT bundle. Further, we assume a constant temperature for the Si substrate denoted as T_s in the equation. This assumption is based on the high thermal conductivity of Si (148 W m^{-1} K^{-1}) as well as the large substrate mass, which can be approximated as semi-infinite medium, compared to the CNT, which yields a negligible substrate temperature rise.

Since the temperature distribution in the SWCNT bundle's cross section is negligible, it is treated by having an effective uniform heat source of $\dot{q}$ in the cross section that varies with

https://doi.org/10.1021/acs.jpcc.3c07572
J. Phys. Chem. C 2024, 128, 1505−1517

the axial direction location to reflect the laser beam Gaussian profile. $\dot{q}$ is defined as

$$\dot{q}(x) = \dot{q}_0 \exp(-x^2/{x_0}^2) \quad (3)$$

where $\dot{q}_0$ is the maximum heat source at the laser beam's center ($x = 0$) and x_0 is the laser beam radius.

Under the above formulation, the SWCNT bundle can be modeled in two equivalent approaches, to some extent. The first approach is to consider the SWCNTs bundle to have a cross-sectional area determined by the nominal diameter, as revealed by the AFM measurements and occupied by individual SWCNTs. By implementing this approach, we shall modify the thermophysical properties to consider the geometry of the individual SWCNTs (cylindrical shells) and hence account for the air gaps. In the second approach, which is the one used in our calculations, we calculate the effective solid cross-sectional area for the bundle as the sum of the solid cross-sectional area for each individual SWCNT. Using this approach, we are permitted to approximate the specific heat as the bulk counterpart, since the effective tube area is considered as a solid rod with no air gaps. The following section will illustrate the method used to reveal the structure of the SWCNT bundle and hence calculate the effective thermophysical properties.

3. RESULTS AND DISCUSSION

3.1. Effective Thermophysical Properties Calculations. Numerical simulation based on the finite-volume method is conducted to solve the heat conduction equation and find the temperature rise under the two energy transport states. In our experiment, since only the RSC ratio of the transient state to the steady state is needed, the absolute temperature rise is not needed. Therefore, an arbitrary $\dot{q}_0$ value is used. In the modeling, the effective cross-sectional area of the bundle is used, and this parameter is obtained based on the Raman spectrum. The RBM bands are commonly used to characterize the SWCNT diameter. However, the RBM spectrum exhibits a complex series of peaks for our sample that presents a challenge for direct analysis. To elucidate the underlying information, a Gaussian multiple peaks function is employed to fit the data as shown in Figure 2d for the first and second locations. The structural analysis as revealed by the AFM and Raman spectrum indicates a uniform sample between locations #1 and #2, which is considered as a constant diameter region in our analysis. Our fitting procedure for both locations revealed five distinct peaks at 109, 127, 143, 166, and 191 cm^{-1} without considering the very tiny peak in the fitting as it is at the noise level of the signal. The diameter of individual SWCNTs inside the bundle is then calculated using the formula $d = A/\omega_{RBM}$, where A is 223.75 (cm^{-1} nm),[31] yielding five distinct SWCNT diameters of 2.05, 1.76, 1.56, 1.35, and 1.17 nm, respectively. As for location #3, the height of the bundle is 4.4 nm, as shown in Figure 1c, larger than the height of the first two locations. Moreover, the RBM spectrum shown in Figure 2e is different from that for the first two locations. This difference in the RBM spectrum is reflected in the multiple peak fitting results, yielding a different distribution of individual SWCNTs inside the bundle. The fitting results for the third location are found to have peaks at 108, 130, 147, 163, 173, and 181 cm^{-1}. The first four peaks (108, 130, 147, and 163 cm^{-1}) are consistent with those found in the first two locations. The discrepancies emerge from the last two peaks (173 and 181 cm^{-1}), which is consistent with the larger bundle size. Using the same procedure mentioned above, the distinct diameters at the third location are calculated to be 2.05, 1.76, 1.56, 1.35, 1.3, and 1.24 nm, respectively. This has significant implications for accurately determining the mass of the bundle, which is directly linked to the determined ITR. Therefore, differentiating the mass of these three locations is a crucial step toward achieving a more precise measurement. The multiple peak fitting procedure is done repeatedly to ensure the uniqueness of the peaks that have emerged and the repeatability of the results of the fitting. The coefficient of determination (R^2) of the fittings shown in Figure 2d,e is computed to be 0.999.

Usually, the Raman signal intensity is proportional to the scattering volume and can be used to assess the volume level under scattering. But for SWCNTs, the RBM excitations are known to be laser dependent; that is, the scattering will become much stronger if the laser energy resonates with the electronic transitions in the one-dimensional electronic density of states. Therefore, the relative Raman intensities of different RBM peaks cannot be used to assess the relative scattering volumes of the SWCNTs of different diameters. Here we use a 785 nm (1.58 eV) laser to obtain the RBM bands and compare them with the bands obtained under a 532 nm (2.33 eV) laser at the third location for its larger size and hence a better signal. The results, as illustrated in Figure 2f, show one major peak at around 172 cm^{-1}, with minor peaks around 101, 109, and 134 cm^{-1} which are more like noises rather than excitations. Since the Raman scattering efficiency is proportional to λ^{-4}, it is understandable that most Raman peaks observed in Figure 2e become very weak under 785 nm excitation. The major peak at 172 cm^{-1} is consistent with the one at 173 cm^{-1} obtained with the 532 nm laser. As mentioned earlier, the sample shows a semiconducting electronic structure, as can be inferred from the Lorentzian shape for the G band. The strong RBM peak under 785 nm laser excitation is more likely induced by the resonant excitation.[42,48,49]

In the literature, two distinct approaches have been proposed to evaluate the cross-sectional area of carbon nanotubes: (i) the entire area enclosed by the outermost carbon nanotube[50] and (ii) the estimated area enclosed by the atoms, calculated as the product of the circumference and thickness of the CNT,[51] where the thickness may fall between 0.142 and 0.34 nm.[52] Our analysis adopts the second approach with the thickness taken as 0.34 nm as it provides more precise estimation of the mass per unit length. Utilizing the nominal diameter of the bundle obtained by AFM, the diameters of individual SWCNTs inside the bundle revealed by the RBM, and the number of individual tubes, we can determine the mass (per unit length) can be determined. The effective cross-sectional area (A_c) of the bundle is calculated for each individual tube as $A_c = (\pi/4)\cdot(d_o^2 - d_i^2)$, where A_c is the effective solid area of a particular tube, d_o is its outer diameter and is revealed by the RBM spectrum, and d_i is its inner diameter ($d_i = d_o - 0.668$ nm). The values are then summed over the number of individual tubes inside the bundle to yield the effective cross-sectional area. As discussed earlier, the first and second locations yield five individual SWCNTs of different diameters, whereas the third location has a larger size and is found to consist of six individual SWCNTs.

Ideally, the structure of the bundle can be best revealed by performing a cross-sectional study using transmission electron microscopy (TEM). However, due to the presence of a large

https://doi.org/10.1021/acs.jpcc.3c07572
J. Phys. Chem. C 2024, 128, 1505−1517

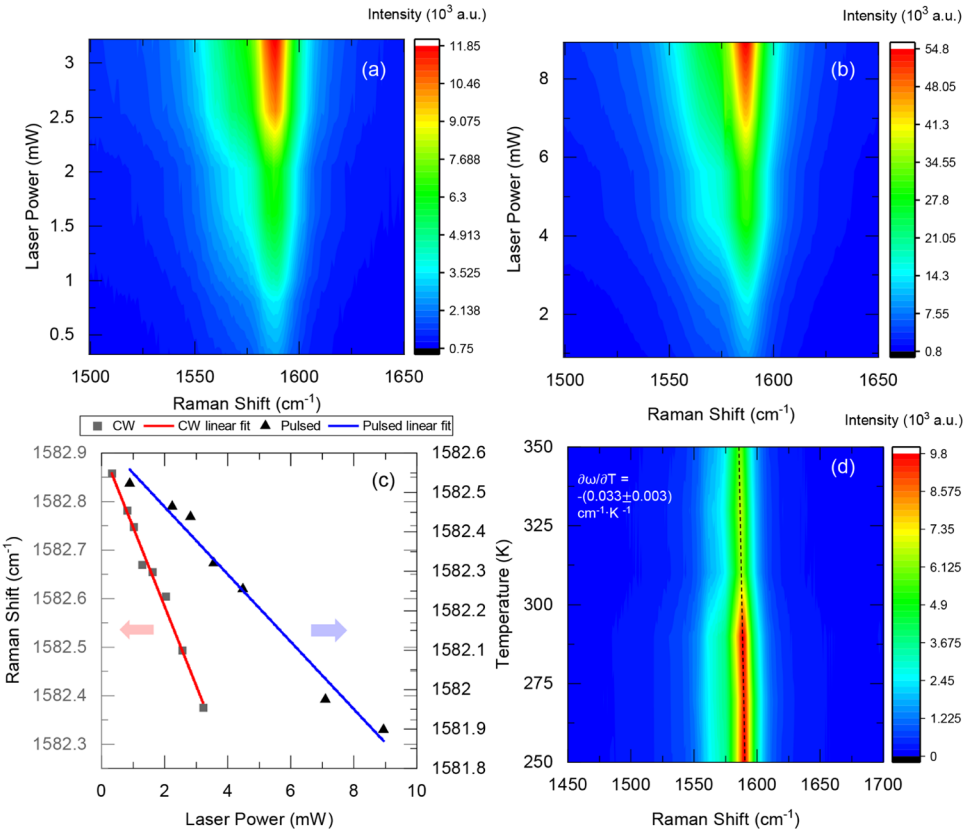

Figure 4. 2D contour for Raman shift variation with laser power at location #3 for (a) CW (i.e., steady state) and (b) pulsed (i.e., transient state). (c) RSC for the CW and pulsed scenarios. (d) 2D contour for Raman shift variation with temperature, with the slope value (i.e., Raman shift temperature coefficient) shown in graph.

number of SWCNT bundles (up to millions within a millimeter size area) on the substrate, it is extremely challenging and nearly impossible to distinguish the sample of interest in a cross-sectional view. Hence, we rely on the RBM excitations and AFM measurements to resolve the structure. The AFM measurements provide confident probing of the sample's height, but it inevitably overestimates the width due to the nature of the scanning process. The apparent width (w) as revealed by AFM measurements is 25.57 and 25.38 nm for the locations with heights of 3.16 and 4.4 nm, respectively. The AFM tip used in the measurement is circular and had a radius of 15 nm. The width measured by AFM is a function of the AFM tip radius and the intrinsic radius of the sample. The exact functional form remains unknown, but we can approximate it using the relation $w \simeq 4(r_{tip} \cdot r_{sample})^{1/2}$ as widely adopted in the literature.[53] Consequently, the sample's width (twice r_{sample}) is determined as 5.44 and 5.36 nm for locations #1 and 2 and #3, respectively.

First, we calculate the effective cross-sectional area, as discussed earlier, at each location considering one individual SWCNT per RBM peak. This is the lowest possible number of SWCNTs that make up the bundle and hence the lowest density (ρ) of the SWCNT bundle. This will yield an upper bound of the ITR calculation as $\rho R'$ is constant inferred from eqs 1 and 2. To assess the uncertainty in our calculations, we then calculate the maximum number of SWCNTs that can fill a rectangular area defined by the height and width as revealed by the AFM. Since this is the maximum packing fraction, we expect to have the lowest possible ITR and hence a lower bound.

3.2. Interfacial Thermal Resistance Determination.

The measured Raman spectrum variation with laser power is shown in Figure 4a,b for steady and transient heating states for location #3. One can clearly notice the red shift as the laser power increases. To quantify the change, we perform a linear fitting, as shown in Figure 4c. The G peak is chosen to probe the thermal response due to its highest signal-to-noise ratio among the entire spectra. At each of the three locations, we obtain ψ_{CW} and ψ_{tr}. It is worth noting that the RSC for a single energy state (i.e., the steady state ψ_{CW} or the transient state ψ_{tr}) is still a function of the laser absorption coefficient (α_L), Raman temperature coefficient ($\partial\omega/\partial T$), and the ITR. In ET-Raman technique, the novelty lies in taking the ratio $\Theta_{exp} = \psi_{tr}/\psi_{CW}$ which cancels out the impact of the laser absorption coefficient and the Raman temperature coefficient for determining the ITR. Therefore, the ITR is the only remaining unknown variable of interest. A more comprehensive discussion on this topic can be found in our previous work.[28]

The relationship between the Raman shift and the laser power for the two energy states for location #3 is illustrated in Figure 4c. A linear dependence is observed, matching our goal, as mentioned earlier. It is also prevalent that the Raman shift in the transient energy state is larger due to a higher laser power. Although the laser power should be of order 1 mW under a 100× objective lens for a CW probing for nanotube bundles due to their poor intertube thermal conductivity as recommended by Dresselhaus et al.[42] The pulse duration in our transient state (20 ns) justifies using higher laser powers. The damage induced can be assessed by the induced temperature increase in the sample. The temperature rise

https://doi.org/10.1021/acs.jpcc.3c07572
J. Phys. Chem. C 2024, 128, 1505−1517

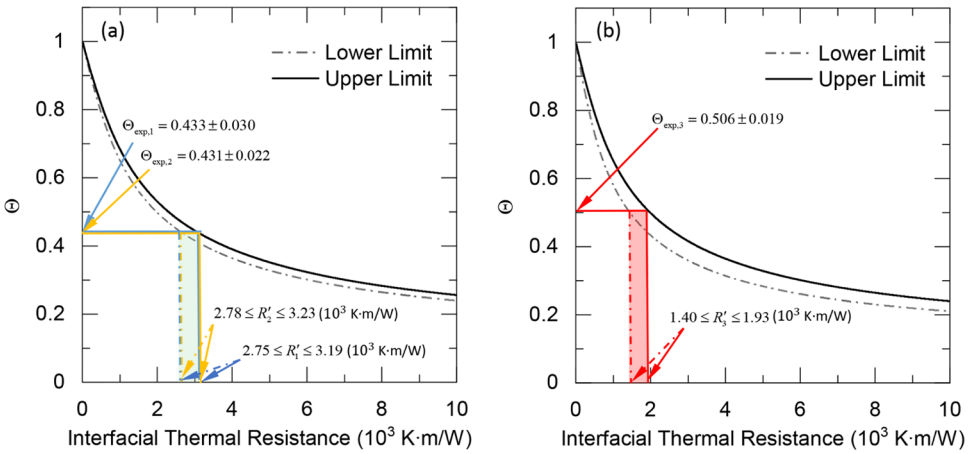

Figure 5. Theoretical weighted temperature rise ratio (Θ) variation with the ITR for (a) location #1 and #2 (b) location #3. The solid line considers the number of individual SWCNTs inside the bundle to be equal to the number of observed peaks in the RBM spectrum which gives the upper bound of the ITR. The dotted-dashed lines consider the maximum possible number of individual SWCNTs that fill the bundle, giving the lower bound of the ITR. The experimental values for Θ_{exp} are mapped on the graph to extract the ITR (R'). The shaded colors represent the uncertainties that mainly arise from the uncertainty in determining the density of the bundle.

induced by the laser heating under CW and amplitude-modulated with nanosecond pulse width are of the same order as will be shown shortly. It is worth mentioning that some of the uncertainties in the final reported ITR arise from the linear peak fitting process. As clearly illustrated in Figure 4c, not all of the data points lie on the linear fitting. This would impact the RSC ratio (Θ_{exp}) that determines the ITR.

In our numerical analysis, we take the constant thermophysical properties of the SWCNT and the substrate. This assumption must be validated by calculating the average temperature increase throughout the experiment to ensure it is small enough to neglect the variations in any of the thermophysical properties. This can be done by measuring the Raman temperature coefficient ($\partial\omega/\partial T$) of the sample, from which the temperature rise in the sample during our measurement can be estimated. Using a heating/cooling stage, the temperature is controlled and varied from 250 to 350 K, and we collect the Raman spectrum along the way. As shown in Figure 4d, the Raman temperature coefficient is determined to be $-(0.033 \pm 0.003)$ cm^{-1} K^{-1}. The average temperature rise can then be calculated as follows: $\Delta T = \Delta\omega/(\partial\omega/\partial T)$, where $\Delta\omega$ is the change in the Raman shift in the experiment. For instance, the highest temperature rise for location #1 under the steady-state condition is estimated to be 13.8 K, whereas it is estimated to be around 18.9 K for the transient state. It is worth noting that due to the very short laser pulse (20 ns) in the transient state, the laser power used for the transient state is much larger than the steady state in order to have a sensitive temperature rise. It is evident that the average temperature rise is within a range that justifies the use of constant thermophysical properties in our data processing.

It should be noted that the experimental RSC ratio (i.e., $\Theta_{exp} = \psi_{tr}/\psi_{CW}$) represents the average temperature increase over the entire measured sample (laser irradiated region). Therefore, the results obtained in our numerical modeling must consider this effect.[54] For the CW scenario, the Raman-intensity weighted average temperature over the sample can be calculated using the following equation: $\Delta\overline{T}_{CW} = \int_0^{x_0} I\Delta T \cdot dx / \int_0^{x_0} I \cdot dx$ where I is the intensity that takes the form $I = I_0 \exp(-x^2/x_0^2)$. For the transient state, the temperature rise is weighted over both time and space as $\Delta\overline{T}_{tr} = \int_0^{t_0}\int_0^{x_0} I\Delta T \cdot dx dt / \int_0^{t_0}\int_0^{x_0} I dx dt$, where t_0 is the laser pulse width (20 ns). The weighted theoretical temperature increase ratio $\Theta = \Delta\overline{T}/\Delta\overline{T}_{CW}$ can be plotted as a function of the ITR (R'). To determine the actual ITR value, we map out the experimental temperature rise ratio in one graph and do data interpolation. Figure 5a shows the ITR for locations 1 and 2, whereas Figure 5b shows the results for location #3. For the first two locations, the nominal dimensions of the SWCNT bundle are almost unchanged as revealed by the AFM and the Raman scanning in Figure 2. The determined value for the ITR is $(2.97 \pm 0.22) \times 10^3$ and $(3.01 \pm 0.23) \times 10^3$ K m W^{-1} for the first and second locations. For the third location, the diameter of the bundle was significantly different, and the ITR is calculated to be $(1.67 \pm 0.27) \times 10^3$ K m W^{-1}. The enhancement in the thermal conductance at the interface of the third location can be attributed to its larger contact area with the substrate as suggested in the literature.[55] These ITR values represent the mean values of the ITR bounded between the upper and lower limits, as illustrated in Figure 5a,b. The uncertainty shown is mainly caused by internal structure analysis of the SWCNT bundle, as explained earlier. A summary of the experimental results, which are taken to be the average of the upper and lower bounds, is given in Table 1.

Table 1. Summary of the Results for the Diameter, Experimental Raman Shift Coefficient Ratio Θ_{exp}, and Measured ITR (R') and the Associated Uncertainty

location	height/width (nm)	Θ_{exp}	R' (10^3 K m W^{-1})	uncertainty (%)
1	3.16/5.44	0.433 ± 0.030	2.97 ± 0.22	7.4
2	3.16/5.44	0.431 ± 0.022	3.01 ± 0.23	7.7
3	4.4/5.36	0.506 ± 0.019	1.67 ± 0.27	16.2

3.3. Discussion on the Measured Interfacial Thermal Resistance. The ITR values reported in previous studies of SWCNT on SiO_2[21] and Sapphire[22] are an order of magnitude lower than those deduced in the present work. It is worth noting that the SWCNT-substrate interfacial resistance dominates the heat dissipation from the nanotubes rather than the specific thermal properties of the different substrates

https://doi.org/10.1021/acs.jpcc.3c07572
J. Phys. Chem. C 2024, 128, 1505−1517

reported above. The previous studies relied on electrical breakdown phenomena, which involved exposing the SWCNT to extremely high temperatures. The interfacial thermal conductance is proportional to the volumetric heat capacity, as both are governed by phonons as the main energy carrier. Both the heat capacity and the interfacial thermal conductance increase with temperature. Hence, the higher temperatures achieved in these studies resulted in higher interfacial conductance (i.e., lower ITR), which could account for the discrepancies. The relationship between ITR (the inverse of the interfacial thermal conductance) and volumetric heat capacity will be discussed in further detail shortly through a qualitative theoretical model. In contrast, the ITR values reported in this study are closer to those reported by Shi et al.[56] for SWCNT on SiO_2. In their work, the joule heating method was used, and the interfacial thermal conductance was estimated to be of order 10^{-3} W m^{-1} K^{-1}, for SWCNT thermal conductivity values between 1000 and 3000 W m^{-1} K^{-1}. These overestimated thermal properties assumed in their calculations, namely, the ultrahigh thermal conductivity, can strongly affect the ITR determination. Our large interfacial resistance is largely caused by the loose contact with the substrate, which might have arisen due to the nonuniformity of the sample as will be discussed shortly. It has previously been demonstrated by Tang et al.[57] that loose contact and the presence of an air gap could reduce the conductance across graphene−Si interfaces by up to 5 orders of magnitude.

We implement a qualitative theoretical model to predict the ITR between the SWCNT bundle and a substrate to better interpret our experimental results. The interfacial resistance can be divided into two parts—one for the direct contact and one for the air gap surrounding the bundle—and is calculated as follows: $R_{tot}' = R_c' \cdot R_{air,gap}'/(R_c' + R_{air,gap}')$, where R_c' is the resistance due to the direct contact and $R_{air,gap}'$ is the resistance due to the air gap surrounding the nanotube. Due to the large mismatch in the group velocities of phonons in carbon nanotubes $\bar{v}_g$ = 13.7 km/s[58] and Si $\bar{v}_g$ = 6.2 km/s,[59] we adopt the diffusive limit for the contact resistance. By employing Chen's model,[60] the interfacial resistance can be calculated as $R_c' = 4/(\alpha_{1\to2} C \cdot \bar{v}_g \cdot a)$, where $\alpha_{1\to2}$ is the transmission coefficient of phonons at the interface, a is the contact width, C is the volumetric heat capacity of carbon nanotubes, and $\bar{v}_g$ is the average group velocity of phonons in the carbon nanotubes. The contact width can be estimated by calculating the deformation of the bundle due to van der Waals forces, which is reported to be between 1 and 3 nm.[61] Given the small diameter of the bundle, we assume a value of 1 nm for order analysis.

The resistance of the air surrounding the bundle can be calculated using the following expression:[55,61]

$$R'_{air,gap} = [2\kappa_{air}\int_a^{D/2}(D/2 - \sqrt{(D^2/4) - x^2} + 2g\lambda_{air})^{-1}\cdot, \mathrm{d}x]^{-1}$$

where κ_{air} is the thermal conductivity of air, D is the diameter of the bundle, λ_{air} is the mean free path of air molecules taken as 68 nm,[62] and g is calculated as $g = 2[(2-\beta)/\beta][2/(\gamma+1)][\kappa_{air}/\mu C_v]$, where γ is the specific heat ratio of air, μ is the air viscosity, C_v is the specific heat of air at constant volume, and β is the accommodation coefficient which measures how efficient the gas molecules transfer the energy as it bounces to/from a solid. By taking β as 0.9,[55] g is calculated to be 2.

The air resistance from the above integral is then calculated to be 4095 K m W^{-1}, a value that is on the order of the measured one in our work. However, in the presence of a direct firm contact between SWCNT and the Si substrate, the heat will always choose the path of least resistance. In other words, this air gap resistance is somewhat irrelevant in the presence of direct and firm contact between the sample and the substrate. As for the direct contact resistance (R_c'), by keeping the phonon transmission coefficient as a free parameter, we estimate the contact ITR per unit length to be of the order of $0.23/\alpha_{1\to2}$. Even under a very poor phonon transmission coefficient, the resistance is still far from the measured one. Thus, we conclude that the bundle likely has loose contact with the substrate. The proposition of a loose contact between the SWCNT bundle and Si substrate might have arisen from the nonuniformity of the sample, as revealed by the AFM and Raman measurements. Our data showed that the bundle has varying diameters along its length, which we anticipate having caused a nonuniform contact with the substrate. Also, as previously mentioned, the type of bonding (covalent vs van der Waal) greatly impacts the interface by 1 order of magnitude.[63] Although the two effects (type of bonding and contact strength) are related to one another, further investigation is needed to determine which is dominant.

By assuming a contact width of 1 nm for order analysis, the ITR per unit area is on the order of 10^{-6} K m^2 W^{-1} for our sample. This "1 nm width" is just an assumption allowing us to estimate the interface thermal resistance per unit area. This is to give a good order estimation and compare with literature data, rather than precise determination. The results are in line with the ITR of mechanically exfoliated graphene and other two-dimensional (2D) materials.[64] For instance, Chen et al.[65] have studied the interfacial thermal conductance between graphene and hexagonal-boron nitride by electrical heating and Raman probing, and the reported result is in the order of 10^6 W m^{-2} K^{-1}. Taube et al.[66] have reported a thermal conductance between MoS_2 monolayers and SiO_2/Si substrate using Raman spectroscopy to be in the range of $(1.25-1.94)\times 10^6$ W m^{-2} K^{-1}, which corresponds to an ITR $\sim 10^{-6}$ K m^2 W^{-1}. Similar results that lie within the same range of the interfacial thermal conductance are reported by Judek et al.[67] for the same interface under consideration, measured using an enhanced opto-thermal technique. The impact of loose contact between graphene and Si, SiO_2,[57] and SiC[68] on the interfacial thermal conductance has been studied comprehensively in our previous work. It has been demonstrated that a loose contact can reduce the interface thermal conductance to the order of 10^3 W m^{-2} K^{-1}.

3.4. Physics of the Interface Energy Transport. The thermal conductance of carbon nanotubes displays a ballistic behavior within a specific range, consistent with theoretical predictions made by Mingo et al.,[69] and was experimentally verified.[51] Notably, the limit at which the heat transfer mechanism transitions from ballistic to diffusive is estimated to be greater than 16 nm at 316 K. These findings suggest that heat transfer in the cross-plane direction of our sample is primarily ballistic, owing to its dimensions being smaller than the phonon mean free path. Several factors can affect the thermal conductance at the interface. The conventional models of phonon transport at material interfaces, such as the acoustic mismatch model (AMM)[70] and diffuse mismatch model (DMM),[71] have primarily focused on the frequency mismatch between the two materials at the bulk scale. However, research

https://doi.org/10.1021/acs.jpcc.3c07572
J. Phys. Chem. C 2024, 128, 1505−1517

by Chen's group has shed new light on the behavior of phonons at the interface.[72] Their findings suggest that phonons at the interface vibrate at higher frequencies than the maximum frequency allowed far from the interface. This implies that the ITR is not solely due to the mismatch in frequency spectra between the materials but also arises from the fact that the high-frequency phonons at the interface correspond to new states that are absent far from the interface. As a result, these phonons must be scattered to match the energy of available states beyond the interface and hence participate in energy transport. This discovery offers a deeper understanding of the underlying mechanisms that govern phonon transport at material interfaces.

Another factor that impacts the conductance at the interface is the surface roughness. While it is commonly believed that surface roughness increases the ITR by promoting diffuse scattering and loss of coherence, recent research has revealed that the influence of surface roughness is not straightforward. In fact, when there is a moderate-to-high mismatch in the acoustic impedance at the interface, surface roughness can have a counterintuitive effect on the thermal resistance. Specifically, when the acoustic impedance changes sharply from high to low at the interface, surface roughness can act as a modifier that smooths this transition, thereby boosting the transmittance of the thermal energy. As a result, the overall effect of surface roughness on the ITR can be ambiguous with the potential for both positive and negative influences. More details can be found in Tian et al.'s[72] work. A similar observation is also reported for graphene−Si interface in Zhang's work.[73] Interestingly, the phenomenon of transmittance enhancement by softening the transition from a high-impedance medium to a low-impedance medium has been previously observed and well established for both photons[74] and electrons.[75]

Efficient heat transfer across interfaces is also determined by the type of bonding between the materials involved. In the case of SWCNT on Si substrate, a covalently bonded interface was found to have an ITR 20 times lower than that of a van der Waal bonded interface.[63] This result is attributed to the enhanced density of low-frequency phonons, specifically the radial breathing mode, in the covalently bonded interface compared with the van der Waal bonded interface. The density of states of tangential modes, which correspond to high-frequency phonons around the G band, showed no significant difference, indicating that longer-wavelength phonons contribute more significantly to heat transfer. It was also noted that van der Waals forces between different nanotubes inside the bundle enhance the interfacial thermal conductance.[76]

4. CONCLUSIONS

In this study, we reported on the interfacial thermal conductance between 1 nm thick SWCNT bundle (3.16 and 4.40 nm heights) and a Si substrate, employing a novel experimental technique developed in our lab: ET-Raman. This technique is highly sensitive by having extremely distinct energy transport states for thermal probing and is highly accurate for eliminating the uncertainties introduced by Raman temperature coefficient determination and laser absorption coefficient measurement. The average temperature rise inside the sample during our ET-Raman measurement was estimated to be 13.8−18.9 K. By comparing the RSC of the two energy transport states to the theoretical values as predicted by solving the heat conduction equation, the interfacial thermal conductance was determined to be in a range of (3.3−6.0) $\times 10^{-4}$ W m^{-1} K^{-1} for three different locations, which corresponds to an interfacial thermal resistance (ITR) of the order 10^{-6} K m^2 W^{-1} for 1 nm contact width, consistent with the previously reported values for ITR for mechanically exfoliated graphene and 2D materials on different substrates. To gain a deeper understanding of our experimental results, we implemented a theoretical model to qualitatively interpret the reported values. Our results suggested that the SWCNT bundle had loose contact with the substrate due to the nonuniformity of the sample, which was investigated and analyzed in comprehensive detail via Raman scanning. Current research efforts in our lab are directed toward characterizing and investigating the temperature dependency of the ITR for SWCNT/SiO_2, which, to the best of our knowledge, has not been investigated in the literature. This is expected to provide great insights to better understand the underlying physics of energy transport for such an interface and will be published in the near future. The current reported results provide valuable insights into the thermal properties of SWCNT/Si interfaces and their implications for applications in various fields such as electronics and energy conversion.

AUTHOR INFORMATION

Corresponding Authors

Baini Li − *Research Center for Industries of the Future, Key Laboratory of 3D Micro/Nano Fabrication and Characterization of Zhejiang Province, School of Engineering, Westlake University, Hangzhou 310024, P. R. China*; Email: libaini@westlake.edu.cn

Tianyu Wang − *Research Center for Industries of the Future, Key Laboratory of 3D Micro/Nano Fabrication and Characterization of Zhejiang Province, School of Engineering, Westlake University, Hangzhou 310024, P. R. China*; Email: wangtianyu79@westlake.edu.cn

Xinwei Wang − *Department of Mechanical Engineering, Iowa State University, Ames, Iowa 50011, United States*; orcid.org/0000-0002-9373-3750; Phone: 001-515-294-8023; Email: xwang3@iastate.edu

Authors

Ibrahim Al Keyyam − *Department of Mechanical Engineering, Iowa State University, Ames, Iowa 50011, United States*

Mahya Rahbar − *Department of Mechanical Engineering, Iowa State University, Ames, Iowa 50011, United States*

Enzheng Shi − *Research Center for Industries of the Future, Key Laboratory of 3D Micro/Nano Fabrication and Characterization of Zhejiang Province, School of Engineering, Westlake University, Hangzhou 310024, P. R. China*; orcid.org/0000-0003-1803-3858

Complete contact information is available at: https://pubs.acs.org/10.1021/acs.jpcc.3c07572

Notes

The authors declare no competing financial interest.

ACKNOWLEDGMENTS

Partial support of this work by the U.S. National Science Foundation (CBET1930866 and CMMI2032464 for X.W.) is gratefully acknowledged.

REFERENCES

(1) Cavin, R. K.; Zhirnov, V. V.; Herr, D. J. C.; Avila, A.; Hutchby, J. Research directions and challenges in nanoelectronics. *J. Nanopart. Res.* **2006**, *8* (6), 841−858.

(2) Avouris, P. Graphene: Electronic and Photonic Properties and Devices. *Nano Lett.* **2010**, *10* (11), 4285−4294.

(3) Biercuk, M. J.; Llaguno, M. C.; Radosavljevic, M.; Hyun, J. K.; Johnson, A. T.; Fischer, J. E. Carbon nanotube composites for thermal management. *Appl. Phys. Lett.* **2002**, *80* (15), 2767−2769.

(4) Xie, Y.; Yuan, P.; Wang, T.; Hashemi, N.; Wang, X. Switch on the high thermal conductivity of graphene paper. *Nanoscale* **2016**, *8* (40), 17581−17597.

(5) Yuan, P.; Li, C.; Xu, S.; Liu, J.; Wang, X. Interfacial thermal conductance between few to tens of layered-MoS_2 and c-Si: Effect of MoS_2 thickness. *Acta Mater.* **2017**, *122*, 152−165.

(6) Rahbar, M.; Han, M.; Xu, S.; Zobeiri, H.; Wang, X. Development of differential thermal resistance method for thermal conductivity measurement down to microscale. *Int. J. Heat Mass Transfer* **2023**, *202*, No. 123712.

(7) Lee, J.-U.; Yoon, D.; Kim, H.; Lee, S. W.; Cheong, H. Thermal conductivity of suspended pristine graphene measured by Raman spectroscopy. *Phys. Rev. B* **2011**, *83* (8), No. 081419.

(8) Geim, A. K.; Novoselov, K. S. The rise of graphene. *Nat. Mater.* **2007**, *6* (3), 183−191.

(9) Balandin, A. A.; Ghosh, S.; Bao, W.; Calizo, I.; Teweldebrhan, D.; Miao, F.; Lau, C. N. Superior Thermal Conductivity of Single-Layer Graphene. *Nano Lett.* **2008**, *8* (3), 902−907.

(10) Schnorr, J. M.; Swager, T. M. Emerging Applications of Carbon Nanotubes. *Chem. Mater.* **2011**, *23* (3), 646−657.

(11) Iijima, S. Helical Microtubules of Graphitic Carbon. *Nature* **1991**, *354* (6348), 56−58.

(12) Hone, J.; Whitney, M.; Piskoti, C.; Zettl, A. Thermal Conductivity of Single-Walled Carbon Nanotubes. *Phys. Rev. B* **1999**, *59* (4), No. R2514.

(13) Zhong, H.; Lukes, J. R. Interfacial Thermal Resistance between Carbon Nanotubes: Molecular Dynamics Simulations and Analytical Thermal Modeling. *Phys. Rev. B* **2006**, *74* (12), No. 125403.

(14) Maruyama, S.; Igarashi, Y.; Taniguchi, Y.; Shiomi, J. Anisotropic Heat Transfer of Single-Walled Carbon Nanotubes. *J. Therm. Sci. Technol.* **2006**, *1* (2), 138−148.

(15) Varshney, V.; Patnaik, S. S.; Roy, A. K.; Farmer, B. L. Modeling of Thermal Conductance at Transverse CNT−CNT Interfaces. *J. Phys. Chem. C* **2010**, *114* (39), 16223−16228.

(16) Shi, J.; Dong, Y.; Fisher, T.; Ruan, X. Thermal transport across carbon nanotube-graphene covalent and van der Waals junctions. *J. Appl. Phys.* **2015**, *118* (4), No. 044302.

(17) Hu, M.; Keblinski, P.; Wang, J.-S.; Raravikar, N. Interfacial thermal conductance between silicon and a vertical carbon nanotube. *J. Appl. Phys.* **2008**, *104* (8), No. 083503.

(18) Yang, J.; Waltermire, S.; Chen, Y.; Zinn, A. A.; Xu, T. T.; Li, D. Contact Thermal Resistance between Individual Multiwall Carbon Nanotubes. *Appl. Phys. Lett.* **2010**, *96* (2), No. 023109.

(19) Velson, N.; Wang, X. Characterization of Thermal Transport across Single-Point Contact between Micro-Wires. *Appl. Phys. A* **2013**, *110* (2), 403−412.

(20) Zhang, C.; Zhao, W.; Bi, K.; Ma, J.; Wang, J.; Ni, Z.; Ni, Z.; Chen, Y. Heat conduction across metal and nonmetal interface containing imbedded graphene layers. *Carbon* **2013**, *64*, 61−66.

(21) Pop, E.; Mann, D. A.; Goodson, K. E.; Dai, H. Electrical and thermal transport in metallic single-wall carbon nanotubes on insulating substrates. *J. Appl. Phys.* **2007**, *101* (9), No. 093710.

(22) Maune, H.; Chiu, H.-Y.; Bockrath, M. Thermal resistance of the nanoscale constrictions between carbon nanotubes and solid substrates. *Appl. Phys. Lett.* **2006**, *89* (1), No. 013109.

(23) Yang, J.; Shen, M.; Yang, Y.; Evans, W. J.; Wei, Z.; Chen, W.; Zinn, A. A.; Chen, Y.; Prasher, R.; Xu, T. T.; et al. Phonon Transport through Point Contacts between Graphitic Nanomaterials. *Phys. Rev. Lett.* **2014**, *112* (20), No. 205901.

(24) Yue, Y.; Zhang, J.; Tang, X.; Xu, S.; Wang, X. Thermal transport across atomic-layer material interfaces. *Nanotechnol. Rev.* **2015**, *4* (6), 533−555.

(25) Beechem, T.; Yates, L.; Graham, S. Invited Review Article: Error and Uncertainty in Raman Thermal Conductivity Measurements. *Rev. Sci. Instrum.* **2015**, *86* (4), No. 041101.

(26) Xu, S.; Fan, A.; Wang, H.; Zhang, X.; Wang, X. Raman-based Nanoscale Thermal Transport Characterization: A Critical Review. *Int. J. Heat Mass Transfer* **2020**, *154*, No. 119751.

(27) Yuan, P.; Wang, R.; Tan, H.; Wang, T.; Wang, X. Energy Transport State Resolved Raman for Probing Interface Energy Transport and Hot Carrier Diffusion in Few-Layered MoS_2. *ACS Photonics* **2017**, *4* (12), 3115−3129.

(28) Wang, R.; Wang, T.; Zobeiri, H.; Yuan, P.; Deng, C.; Yue, Y.; Xu, S.; Wang, X. Measurement of the thermal conductivities of suspended MoS_2 and $MoSe_2$ by nanosecond ET-Raman without temperature calibration and laser absorption evaluation. *Nanoscale* **2018**, *10* (48), 23087−23102.

(29) Zobeiri, H.; Wang, R.; Wang, T.; Lin, H.; Deng, C.; Wang, X. Frequency-domain energy transport state-resolved Raman for measuring the thermal conductivity of suspended nm-thick $MoSe_2$. *Int. J. Heat Mass Transfer* **2019**, *133*, 1074−1085.

(30) Hou, J.; Wang, X.; Vellelacheruvu, P.; Guo, J.; Liu, C.; Cheng, H.-M. Thermal characterization of single-wall carbon nanotube bundles using the self-heating 3ω technique. *J. Appl. Phys.* **2006**, *100* (12), No. 124314.

(31) Fatahi-Vajari, A.; Imam, A. Analysis of Radial Breathing Mode of Vibration of Single-Walled Carbon Nanotubes via Doublet Mechanics. *ZAMM - J. Appl. Math. Mech./Z. Angew. Math. Mech.* **2016**, *96* (9), 1020−1032.

(32) Meyer, J. C.; Paillet, M.; Michel, T.; Moréac, A.; Neumann, A.; Duesberg, G. S.; Roth, S.; Sauvajol, J.-L. Raman Modes of Index-Identified Freestanding Single-Walled Carbon Nanotubes. *Phys. Rev. Lett.* **2005**, *95* (21), No. 217401.

(33) Milnera, M.; Kürti, J.; Hulman, M.; Kuzmany, H. Periodic Resonance Excitation and Intertube Interaction from Quasicontinuous Distributed Helicities in Single-Wall Carbon Nanotubes. *Phys. Rev. Lett.* **2000**, *84* (6), No. 1324.

(34) Jorio, A.; Saito, R.; Hafner, J. H.; Lieber, C. M.; Hunter, M.; McClure, T.; Dresselhaus, G.; Dresselhaus, M. S. Structural (n,m) Determination of Isolated Single-Wall Carbon Nanotubes by Resonant Raman Scattering. *Phys. Rev. Lett.* **2001**, *86* (6), No. 1118.

(35) Fantini, C.; Jorio, A.; Souza, M.; Strano, M. S.; Dresselhaus, M. S.; Pimenta, M. A. Optical Transition Energies for Carbon Nanotubes from Resonant Raman Spectroscopy: Environment and Temperature Effects. *Phys. Rev. Lett.* **2004**, *93* (14), No. 147406.

(36) Jorio, A.; Filho, A. G. S.; Dresselhaus, G.; Dresselhaus, M. S.; Swan, A. K.; Ünlü, M. S.; Goldberg, B. B.; Pimenta, M. A.; Hafner, J. H.; Lieber, C. M.; Saito, R. G-band Raman Spectra of Isolated Single Wal Carbon Nanotubes: Diameter and Chiraity Dependence. *MRS Proc.* **2001**, *706*, No. 6191.

(37) Dresselhaus, M. S.; Dresselhaus, G.; Jorio, A.; Filho, A. G. S.; Saito, R. Raman spectroscopy on isolated single wall carbon nanotubes. *Carbon* **2002**, *40* (12), 2043−2061.

(38) Pimenta, M. A.; Jorio, A.; Brown, S. D. M.; Filho, A. G. S.; Dresselhaus, G.; Hafner, J. H.; Lieber, C. M.; Saito, R.; Dresselhaus, M. S. Diameter dependence of the Raman D band in isolated single-wall carbon nanotubes. *Phys. Rev. B* **2001**, *64* (4), No. 041401.

(39) Ferrari, A. C. Raman spectroscopy of graphene and graphite: Disorder, electron−phonon coupling, doping and nonadiabatic effects. *Solid State Commun.* **2007**, *143* (1), 47−57.

(40) Ferrari, A. C.; Robertson, J. Interpretation of Raman spectra of disordered and amorphous carbon. *Phys. Rev. B* **2000**, *61* (20), No. 14095.

(41) Shimada, T.; Sugai, T.; Fantini, C.; Souza, M.; Cançado, L. G.; Jorio, A.; Pimenta, M. A.; Saito, R.; Grüneis, A.; Dresselhaus, G.; et al. Origin of the 2450 cm−1 Raman bands in HOPG, single-wall and double-wall carbon nanotubes. *Carbon* **2005**, *43* (5), 1049−1054.

https://doi.org/10.1021/acs.jpcc.3c07572
J. Phys. Chem. C 2024, 128, 1505−1517

(42) Dresselhaus, M. S.; Dresselhaus, G.; Saito, R.; Jorio, A. Raman Spectroscopy of Carbon Nanotubes. *Phys. Rep.* **2005**, *409* (2), 47−99.
(43) Simon, S. H. *The Oxford Solid State Basics*; Oxford University Press, 2013.
(44) Zou, J.; Ji, B.; Feng, X.-Q.; Gao, H. Self-Assembly of Single-Walled Carbon Nanotubes into Multiwalled Carbon Nanotubes in Water: Molecular Dynamics Simulations. *Nano Lett.* **2006**, *6* (3), 430−434.
(45) Yuzvinsky, T. D.; Mickelson, W.; Aloni, S.; Begtrup, G. E.; Kis, A.; Zettl, A. Shrinking a Carbon Nanotube. *Nano Lett.* **2006**, *6* (12), 2718−2722.
(46) Incropera, F.; Dewitt, D.; Bergman, T.; Lavine, A. *Fundamentals of Heat and Mass Transfer*; John Wiley, 2007.
(47) Rahbar, M.; Li, B.; Hunter, N.; Al Keyyam, I.; Wang, T.; Shi, E.; Wang, X. Observing grain boundary-induced phonons mean free path in highly aligned SWCNT bundles by low-momentum phonon scattering. *Cell Rep. Phys. Sci.* **2023**, *4*, No. 101688.
(48) Dresselhaus, M. S.; Dresselhaus, G.; Jorio, A. Unusual Properties and Structure of Carbon Nanotubes. *Annu. Rev. Mater. Res.* **2004**, *34* (1), 247−278.
(49) Kataura, H.; Kumazawa, Y.; Maniwa, Y.; Umezu, I.; Suzuki, S.; Ohtsuka, Y.; Achiba, Y. Optical Properties of Single-Wall Carbon Nanotubes. *Synth. Met.* **1999**, *103* (1), 2555−2558.
(50) Fujii, M.; Zhang, X.; Xie, H.; Ago, H.; Takahashi, K.; Ikuta, T.; Abe, H.; Shimizu, T. Measuring the Thermal Conductivity of a Single Carbon Nanotube. *Phys. Rev. Lett.* **2005**, *95* (6), No. 065502.
(51) Yu, C.; Shi, L.; Yao, Z.; Li, D.; Majumdar, A. Thermal Conductance and Thermopower of an Individual Single-Wall Carbon Nanotube. *Nano Lett.* **2005**, *5* (9), 1842−1846.
(52) Yao, Z.; Wang, J.-S.; Li, B.; Liu, G.-R. Thermal conduction of carbon nanotubes using molecular dynamics. *Phys. Rev. B* **2005**, *71* (8), No. 085417.
(53) Winzer, A. T.; Kraft, C.; Bhushan, S.; Stepanenko, V.; Tessmer, I. Correcting for AFM Tip Induced Topography Convolutions in Protein−DNA Samples. *Ultramicroscopy* **2012**, *121*, 8−15.
(54) Hunter, N.; Rahbar, M.; Wang, R.; Mahjouri-Samani, M.; Wang, X. Determination of a Raman Shift Laser Power Coefficient based on Cross Correlation. *Opt. Lett.* **2022**, *47* (24), 6357−6360.
(55) Prasher, R. Predicting the Thermal Resistance of Nanosized Constrictions. *Nano Lett.* **2005**, *5* (11), 2155−2159.
(56) Shi, L.; Zhou, J.; Kim, P.; Bachtold, A.; Majumdar, A.; McEuen, P. L. Thermal probing of energy dissipation in current-carrying carbon nanotubes. *J. Appl. Phys.* **2009**, *105* (10), No. 104306.
(57) Tang, X.; Xu, S.; Zhang, J.; Wang, X. Five orders of magnitude reduction in energy coupling across corrugated graphene/substrate interfaces. *ACS Appl. Mater. Interfaces* **2014**, *6* (4), 2809−2818.
(58) Dresselhaus, M. S.; Eklund, P. C. Phonons in carbon nanotubes. *Adv. Phys.* **2000**, *49*, 705−814.
(59) Pop, E.; Dutton, R. W.; Goodson, K. E. Analytic band Monte Carlo model for electron transport in Si including acoustic and optical phonon dispersion. *J. Appl. Phys.* **2004**, *96* (9), 4998−5005.
(60) Chen, G. Thermal Conductivity and Ballistic-Phonon Transport in the Cross-Plane Direction of Superlattices. *Phys. Rev. B* **1998**, *57* (23), No. 14958.
(61) Bahadur, V.; Xu, J.; Liu, Y.; Fisher, T. S. Thermal Resistance of Nanowire-Plane Interfaces. *J. Heat Transfer* **2005**, *127* (6), 664−668.
(62) Jennings, S. G. The mean free path in air. *J. Aerosol Sci.* **1988**, *19* (2), 159−166.
(63) Osman, M. A.; Kim, T. Thermal Interface Resistance Between Silicon and Single Wall Carbon Nanotubes. In *Nanotube Superfiber Materials*, 2nd ed.; Schulz, M. J.; Shanov, V.; Yin, Z.; Cahay, M., Eds.; William Andrew Publishing, 2019; pp 603−621.
(64) Yue, Y.; Zhang, J.; Xie, Y.; Chen, W.; Wang, X. Energy coupling across low-dimensional contact interfaces at the atomic scale. *Int. J. Heat Mass Transfer* **2017**, *110*, 827−844.
(65) Chen, C.-C.; Li, Z.; Shi, L.; Cronin, S. B. Thermal interface conductance across a graphene/hexagonal boron nitride heterojunction. *Appl. Phys. Lett.* **2014**, *104* (8), No. 081908.
(66) Taube, A.; Judek, J.; Łapińska, A.; Zdrojek, M. Temperature-Dependent Thermal Properties of Supported MoS2Monolayers. *ACS Appl. Mater. Interfaces* **2015**, *7* (9), 5061−5065.
(67) Judek, J.; Gertych, A. P.; Świniarski, M.; Łapińska, A.; Dużyńska, A.; Zdrojek, M. High accuracy determination of the thermal properties of supported 2D materials. *Sci. Rep.* **2015**, *5* (1), No. 12422.
(68) Tang, X.; Xu, S.; Wang, X. Corrugated epitaxial graphene/SiC interfaces: photon excitation and probing. *Nanoscale* **2014**, *6* (15), 8822−8830.
(69) Mingo, N.; Broido, D. A. Carbon Nanotube Ballistic Thermal Conductance and Its Limits. *Phys. Rev. Lett.* **2005**, *95* (9), No. 096105.
(70) Little, W. A. The Transport of Heat between Dissimilar Solids at Low Temperatures. *Can. J. Phys.* **1959**, *37* (3), 334−349.
(71) Swartz, E. T.; Pohl, R. O. Thermal Boundary Resistance. *Rev. Mod. Phys.* **1989**, *61* (3), No. 605.
(72) Tian, Z.; Esfarjani, K.; Chen, G. Enhancing Phonon Transmission across a Si/Ge Interface by Atomic Roughness: First-principles Study with the Green's Function Method. *Phys. Rev. B* **2012**, *86* (23), No. 235304.
(73) Zhang, J.; Wang, Y.; Wang, X. Rough contact is not always bad for interfacial energy coupling. *Nanoscale* **2013**, *5* (23), 11598−11603.
(74) Huang, Y.-F.; Chattopadhyay, S.; Jen, Y.-J.; Peng, C.-Y.; Liu, T.-A.; Hsu, Y.-K.; Pan, C.-L.; Lo, H.-C.; Hsu, C.-H.; Chang, Y.-H.; et al. Improved Broadband and quasi-omnidirectional Anti-reflection Properties with Biomimetic Silicon Nanostructures. *Nat. Nanotechnol.* **2007**, *2* (12), 770−774.
(75) Tai, K.; Yang, L.; Wang, Y. H.; Wynn, J. D.; Cho, A. Y. Drastic reduction of series resistance in doped semiconductor distributed Bragg reflectors for surface-emitting lasers. *Appl. Phys. Lett.* **1990**, *56* (25), 2496−2498.
(76) Feng, Y.; Zhu, J.; Tang, D. Effect of van der Waals forces on thermal conductance at the interface of a single-wall carbon nanotube array and silicon. *AIP Adv.* **2014**, *4* (12), No. 127118.

https://doi.org/10.1021/acs.jpcc.3c07572
J. Phys. Chem. C 2024, 128, 1505−1517